Solar Aircraft Design Trade Studies Using Geometric Programming

Michael Burton[*], Christopher Courtin[†], Mark Drela[‡]
Dorian Colas[§], Nicholas Roberts[¶], Vishvas Suryakumar[‖]

Solar aircraft design is a multidisciplinary problem in which tradeoffs between aerodynamic performance, structural integrity, component performance, cost, and manufacturability are complex and non-intuitive. By formulating the problem as a Geometric Program, design configuration trades and parameter sensitivity studies can be achieved with far greater speed and reliability than possible using more traditional conceptual and preliminary aircraft design practices. Using the GP approach, trade studies in design parameters, configurations and requirements are presented for an optimized solar-electric aircraft. The results of these trade studies are used to inform design decisions and validate higher order models.

Nomenclature

AR	wing aspect ratio		L_h	horizontal tail lift
B	number of propeller blades		L_w	wing lift
b	wing span		l_pod	pod length
c	wing chord		l_h	horizontal tail moment arm
C_f	skin friction coefficient		M_cg	moment about center of mass
C_L	lift coefficient		q	freestream dynamic pressure
C_{L_0}	zero-α lift coefficient		N	load factor
C_{L_h}	horizontal tail lift coefficient		N_gust	gust load factor
$C_{L_{h_0}}$	zero-α horizontal tail lift coefficient		Q	prop torque
C_m	moment coefficient		Q_motor	motor torque
ΔW	wing section weight		R_pod	pod radius
Δy	wing section length		R	propeller radius
e	span efficiency factor		R_motor	motor resistance
E	Young's Modulus		Re	Reynolds number
E_batt	energy stored in battery		S	reference area (wing planform area)
g	gravitational constant		S_pod	pod wetted surface area
h	flight altitude		S_h	horizontal tail planform area
h_batt	battery specific energy		SM_min	minimum static margin
h_cap	spar cap separation		$\mathcal{S}$	shear load
i	motor current		t_cap	spar cap thickness
i_0	motor zero-load current		t_core	spar core thickness
I	spar-section area moment of inertia		t_shear	shear web thickness
I_0	tailboom root section area moment of inertia		$\mathcal{T}$	torsion load
K_V	electric motor speed constant		V	true airspeed
k	tailboom taper index		$\mathcal{V}_\mathrm{pod}$	pod volume
k_pod	pod pressure-drag form factor		V_h	horizontal tail volume

[*]PhD Student, MIT Dept. of Aeronautics and Astronautics, 77 Mass Ave, Cambridge MA, 02139, AIAA Student.

[†]PhD Student, MIT Dept. of Aeronautics and Astronautics, 77 Mass Ave, Cambridge MA, 02139, AIAA Student.

[‡]Terry J. Kohler Professor, MIT Dept. of Aeronautics and Astronautics, 77 Mass Ave, Cambridge MA, 02139, AIAA Fellow.

[§]Airframe Design Lead, Facebook, 1 Hacker Way, Menlo Park CA, 94025

[¶]Airframe Optimization Engineer, Facebook, 1 Hacker Way, Menlo Park CA, 94025

[‖]Airframe Structural Engineer, Facebook, 1 Hacker Way, Menlo Park CA, 94025

American Institute of Aeronautics and Astronautics Paper 2018-XXXX

v	motor voltage	Γ	prop blade circulation
v_a	prop axial induced velocity	ϵ	downwash angle
v_t	prop tangential induced velocity	η_{charge}	battery charging efficiency
W_a	prop blade-relative axial velocity	$\eta_{\text{discharge}}$	battery discharging efficiency
W_t	prop blade-relative tangential velocity	η_{prop}	propulsive efficiency
W_{batt}	battery weight	η_{solar}	solar cell efficiency
w_{cap}	spar cap width	θ	wing deflection angle
W_{pod}	pod weight	ϕ	wing twist angle
W_{h}	horizontal tail weight	$\rho_{A_{\text{cfrp}}}$	area density of carbon fiber
w_{max}	maximum deflection limit	ρ_{cfrp}	density of carbon fiber
W_{MTO}	max take-off weight	ρ_{foam}	density of foam
W_{pay}	payload weight	σ_{cfrp}	maximum carbon fiber stress
W_{spar}	wing spar weight	τ_t	wing thickness to chord ratio
W_{wing}	wing weight	τ_w	cap spar width to chord ratio
x_{cg}	center of gravity	Ω	propeller rotation rate
x_{ac}	aerodynamic center	Ω_{motor}	motor rotation rate
α	angle of attack		

I.   Introduction

Solar-electric, high-altitude, long-endurance (HALE) aircraft are being investigated and developed to serve as effective communication-relay platforms [1]. The basic concept is that during the day the aircraft gathers solar energy, part of which is used for propulsion and the rest is stored in batteries, and the battery energy is then used for propulsion during the night. A major difficulty with such aircraft is that they require extreme aerodynamic and propulsive efficiencies, and very high solar cell efficiencies and battery specific energies for the design to achieve energy closure. Another source of difficulty is the multifaceted and non-intuitive interactions between aerodynamics, structural weight, solar energy collection, and flight-environment factors [2]. This complexity makes exhaustive evaluation of Solar HALE configuration options difficult or impractical if traditional ad-hoc design space investigation procedures are used.

An established approach to complex aircraft design problems is Multidisciplinary Design Optimization (MDO) [3]. MDO methods typically consist of a collection of discipline-specific modules (aerodynamics, structures, propulsion, etc.) each of which has a specific set of inputs and outputs, with the inputs provided by the design problem or from the outputs of another module. Hence, the input/output sequence of all the modules must be set during problem formulation. However, in a tightly-coupled design problem the distinction between inputs and outputs is often not clear. For example, should the spar-stress equations be used to size the spar material gauges and thus the spar weight for a given airload and wingspan, or should they be used to size the wingspan for a given airload and spar weight budget? An MDO method typically resolves this ambiguity by iteration so that some combination of spar weight and span is the final result. But if the a priori chosen input/output sequence is nearly in the "wrong direction" (i.e. the span is imposed on the spar-stress model but in reality the model strongly dictates the span), then the MDO design iteration convergence will be very slow or may even fail.

An alternative to traditional MDO, particularly in the conceptual design phase, is the geometric programming (GP) modeling approach. This is described by Hoburg and Abbeel [4] for general aircraft design, and more recently by Burton and Hoburg [5] for the Solar HALE problem. In summary, a GP method is a collection of constraint equations expressed in terms of design variables and design parameters, but unlike MDO it does not require the definition of equation inputs and outputs, nor does it require a specific equation application sequence. Hence it is more natural to apply in complex and tightly-coupled design problems such as Solar HALE, where such variable and equation-application hierarchies are not obvious at the outset.

A soft barrier to the use of GP is that it typically requires higher fidelity models to be approximated as convex constraints [4]. However, this paper will show that for the Solar HALE problem this barrier is not a major impediment, and that even fairly complex models can be formulated in the necessary GP form.

One very strong benefit of the GP approach is its speed and reliability. Because GPs can solve for thousands of variables in seconds [6], a very large number of potential designs and configurations can be examined and evaluated. In addition to giving the optimal solution, GP provides post-optimum sensitivities to every design parameter as a by-product, with negligible additional cost. This allows for immediate identification of driving design parameters, which informs design decisions on further development and

refinement. More exhaustive conceptual design then allows definition of a relatively robust design as the starting point for the higher-fidelity methods used in subsequent preliminary and detailed design procedures. This paper will illustrate these capabilities for the Solar HALE design problem. The focus will be on modeling refinements from the work of Burton and Hoburg [5], to demonstrate that higher fidelity models can be written in a GP form and used to capture important physical effects and corresponding design tradeoffs. The specific model refinements include spanwise-distributed battery pods, effects of tailboom flexibility on pitch stability, and a coupled propeller+motor performance and weight model.

II. Solar HALE Baseline Design

The basic assumptions of the GP model of Burton and Hoburg are summarized as follows:

- Configuration: The wing is assumed to have a constant taper, and a conventional aft tail is used. The batteries are placed inside the wing to achieve span loading. Solar panels are placed on the wing only.

- Operations: The aircraft is assumed to fly above $50,000\,$ft to avoid cloud coverage and to reach the local minimum wind speeds that occur around $60,000\,$ft [5]. The model trades air density with wind speed to achieve the optimum altitude. Solar flux is calculated as a function of latitude and day of the year and assumes the wing is flat.

- Structural: The aircraft is subjected to two load cases: a standard g-loading and a spanwise 1–cosine distribution gust load. The wing spar is assumed to take all of the bending loads and is a cap spar with a shear/torsion wrap. The tailboom is a tube with a linearly-tapered wall thickness. All materials are carbon fiber and foam, with non-structural surface skins.

The GP model of Burton and Hoburg captures trade offs between latitude, altitude, required battery size, solar panels and overall aircraft size. The higher fidelity changes to be presented here include:

- Wing torsional divergence analysis to capture the tradeoff between wing aspect ratio and the weight of the spar torsion material.

- Battery pods along the wing to capture the trade off between outboard bending relief on the wings and the added weight and drag of the pods.

- Tailboom flexibility resulting in decreased horizontal tail effectiveness, to capture the tradeoff between tailboom weight and horizontal tail weight and drag.

- Refined solar flux model to capture trade off between season requirement and aircraft size.

- Expanded airfoil data fitting to capture the airfoil thickness-related trade offs between structural merit and profile drag.

- Motor and propeller matching to capture the trade off between motor weight and propeller efficiency and weight for multiple operating scenarios.

For a given set of requirements (Table 1) and baseline assumptions (Table 2), this comprehensive GP model is solved for 702 variables in 0.187 seconds on a desktop computer. One benefit of GP models is that any design parameter can be changed and the model resolved in a fraction of a second. Table 2 shows a partial list of design parameters that can be changed, with each change resulting in a new re-optimized aircraft. These design parameter values are generally representative of current technology, and were chosen as a suitable baseline for the refined models and parameter studies to be presented.

Table 1: Mission Requirements

Requirement	Value
Station Keeping	90% winds
Season	all seasons
Latitude	$\pm 20^\circ$

Table 2: Typical design parameter values and resulting design variables

Design Parameter	Specified Value
W_{pay}	10 lb
$\eta_{\mathrm{charge,discharge}}$	0.98
h_{batt}	350 Whr/kg
η_{solar}	0.22
N_{max}	2
N_{safety}	1.5
e	0.95

Design Variable	Optimum Value
W_{MTO}	436 lbf
W_{batt}	244 lbf
W_{wing}	67.9 lbf
AR	38.1
b	123 ft
V	22.9 m/s
C_L	1.3

III. Sensitivity Analysis

In geometric programming the sensitivity to a parameter is defined as the percentage change in the objective function for a corresponding one percent change in that parameter value. For the present example, the sensitivity to battery specific energy h_{batt} is -4.74, so that if the battery specific energy were increased by 1% this would result in a 4.74% decrease in the aircraft total weight. Sensitivities are local approximations in that they will change along a parameter sweep, but they are nevertheless useful for understanding relative parameter importance. Figure 1 shows the largest-magnitude sensitivities for the design parameters in Table 2.
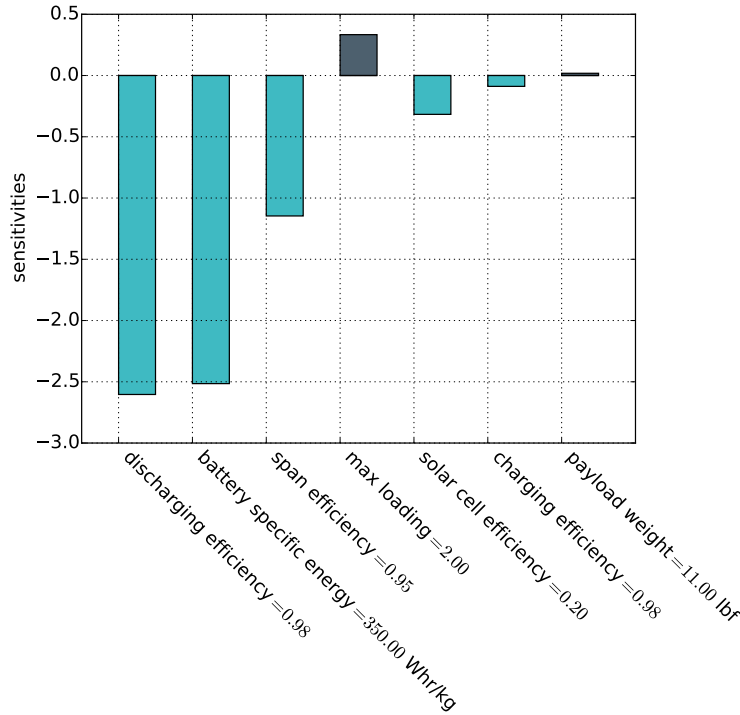
Figure 1: Parameters with highest sensitivity have largest effect on objective function.

These sensitivities can help identify the most important aspects of a design. In this Solar HALE example, the sensitivity of the gross weight to the payload weight is less than unity, which is most likely due to the Reynolds number benefit of larger aircraft size. In contrast, the sensitivities to the propeller efficiency, battery specific energy and solar cell efficiency are all far above unity. This suggests that higher fidelity models should be used, if possible, to better estimate the performance of these components to meet the

design requirements.

Another useful application for sensitivities is to evaluate return on investment costs of improving technology. Batteries and solar cells both have high costs, but it is not immediately obvious which one, if improved, will have greater impact on reduction of aircraft size and weight. If it is assumed that the cost of improving solar cells and the cost of improving batteries for a given percentage are the same, then by using the sensitivities it becomes clear that investing in battery technology will have a greater impact on the design than by investing in solar cells.

IV. Configuration Trade Studies

A. Spar Configuration and Twist Load Calculation

The model of Burton and Hoburg assumes a simple foam-filled box spar consisting of sparcaps and a shear wrap. The foam is needed to stabilize the sparcaps against buckling, but adds significant weight. This section presents an alternative hollow box spar, shown in Figure 2, in which each sparcap is a thin sandwich to provide the cap with its own bending stiffness for buckling resistance. A separate torsion analysis will also be presented to effectively size the shear wrap.
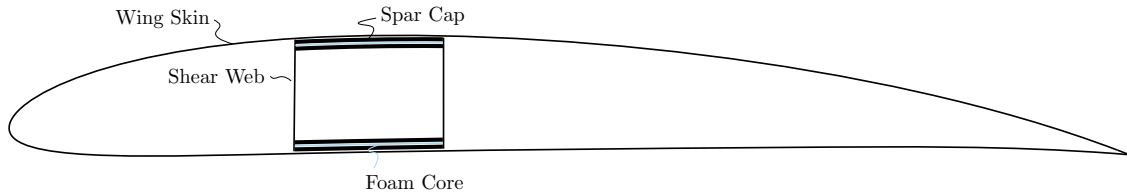
Figure 2: Cross sectional view of a box spar.

A characteristic feature of GP modeling is that model equalities become replaced with inequality constraints, so that the problem is put into the form required by the GP solver. For example, the spar's local bending inertia is defined by the constraint

$$I_i \leq w_{\mathrm{cap}_i} t_{\mathrm{cap}_i} h_{\mathrm{cap}_i}^2 \tag{1}$$

and the solver will then drive the I_i variable onto the constraint boundary since that is most favorable, and thus we recover the equality. Similarly, the defining constraint for the weight of a spanwise Δy_i spar section is

$$\Delta W_i \geq g \left[\rho_{\mathrm{cfrp}} \left(4 w_{\mathrm{cap}_i} t_{\mathrm{cap}_i} + 2 t_{\mathrm{shear}_i} (h_{\mathrm{cap}_i} + 4 t_{\mathrm{cap}_i} + 2 t_{\mathrm{core}_i}) \right) + 2 \rho_{\mathrm{foam}} w_{\mathrm{cap}_i} t_{\mathrm{core}_i} \right] \Delta y_i \tag{2}$$

Additional geometric constraints are imposed on the width and thickness for both the cap spar and box spar configurations. For example, the overall spar height cannot exceed the airfoil thickness, and the spar width cannot exceed a specified fraction τ_w of the chord.

$$h_{\mathrm{cap}_i} + 4 t_{\mathrm{cap}_i} + 2 t_{\mathrm{core}} \leq c_i \tau_t \tag{3}$$

$$w_{\mathrm{cap}_i} \leq c_i \tau_w \tag{4}$$

Burton and Hoburg consider two loading cases in their model: a standard g-loading and a spanwise 1–cosine gust load. The spar must meet both strength and stiffness constraints for both load cases. The sparcap stress must be below the max allowable stress for unidirectional carbon fiber, assumed here to be $\sigma_{\mathrm{cfrp}} = 1500\,\mathrm{MPa}$ [7]. The tip deflection at max load is constrained to be less than 20% of the half span, $w_{\mathrm{max}}/(b/2) = 0.2$, with this value picked here somewhat arbitrarily. In general, only one of these constraints will be active in the optimum solution returned by the GP solver.

An additional constraint is added to limit the maximum twist deflection of the wing to some value (here assumed 15° at the tip), to prevent aeroelastic torsional divergence at the never-exceed dynamic pressure q_{NE}. This in effect sizes the spar's polar moment of inertia J, related to the shear wrap geometry by the constraint

$$J_i \leq \frac{t_i \, w_{\mathrm{cap}_i} \, t_{\mathrm{shear}_i}}{3} (t_i + w_i). \tag{5}$$

American Institute of Aeronautics and Astronautics Paper 2018-XXXX

The spanwise torsion loads $\mathcal{T}_i$ and twist angles ϕ_i, defined positive nose down, are defined by the beam-torsion model constraints

$$\mathcal{T}_{i+1} \;\geq\; \mathcal{T}_i \;-\; c_m\, q_{NE}\, \frac{c_{i+1}^2 + c_i^2}{2}\, \Delta y \tag{6}$$

$$\phi_{i+1} \;\geq\; \phi_i \;+\; \frac{1}{2}\left(\frac{\mathcal{T}_{i+1}}{GJ_{i+1}} + \frac{\mathcal{T}_i}{GJ_i}\right)\Delta y \tag{7}$$

where q_{NE} is the never exceed dynamic pressure and c_m is the airfoil pitching moment. The aerodynamic torsion load term in (6) does not include the contribution of the lift, but at q_{NE} this is usually relatively small compared to the c_m term. Furthermore, for the usual negative c_m the lift would also reduce the torsion load so omitting it is a conservative approximation.

This model captures the tradeoff between wing aspect ratio and the weight of the spar torsion wrap thickness and weight. Table 3 shows that the twist constraint drives down the optimum aspect ratio as expected, and also results in a substantial design penalty in the form of increased gross weight and span.

Table 3: Effect of Twist Constraint

Variable	Baseline Value	With Twist Constraint
W_{MTO}	436 lbf	525 lbf
W_{wing}	67.9 lbf	96.7 lbf
W_{spar}	39.7 lbf	63.7 lbf
AR	38.1	36
b	123 ft	129 ft

B.   Battery Placement Trade Study

For a solar aircraft, placing the batteries inside the wings achieves a span-loaded weight distribution and allows for overall lower bending moments on the aircraft. Additionally, this configuration will have less drag and weight than if the batteries were placed in pods along the wing. However, for ease of manufacturing and battery swapping, it is desirable to place the batteries in pods along the span of the wing. A trade study between number of pods and overall aircraft weight is accomplished by modeling the pods as ellipsoids and accounting for the bending relief of those pods if placed along the span.

The volume of an ellipsoid pod is constrained by the volume of the battery

$$\mathcal{V}_{\mathrm{pod}} \;\geq\; \frac{E_{\mathrm{batt}}}{V_{\mathrm{batt}}} \tag{8}$$

where E_{batt} is the required battery energy to operate through the duration of the night on the winter's solstice and $V_{\mathrm{batt}} = 800\,\mathrm{Whr/l}$ is the battery energy density. The dimensions of the pod are constrained by

$$\mathcal{V}_{\mathrm{pod}} \;\leq\; \frac{4}{3}\pi\, \frac{l_{\mathrm{pod}}}{2}\, R_{\mathrm{pod}}^2 \tag{9}$$

where l_{pod} is the length of the pod and R_{pod} is the radius. Using the length and radius, the surface area can be calculated using Thomsen's approximation,[8]

$$3\left(\frac{S_{\mathrm{pod}}}{\pi}\right)^{1.6075} \;\geq\; 2\,(2 l_{\mathrm{pod}} R_{\mathrm{pod}})^{1.6075} + (4 R_{\mathrm{pod}}^2)^{1.6075}. \tag{10}$$

The weight of the pod is defined by the constraint

$$W_{\mathrm{pod}} \;\geq\; S_{\mathrm{pod}}\, \rho_{A_{\mathrm{cfrp}}}\, g \tag{11}$$

where $\rho_{A_{\mathrm{cfrp}}} = 0.243\,\mathrm{g/cm}^2$, or the area density of about 5 plies of carbon fiber.[9] The surface area is also used to calculate the drag assuming a skin friction based drag model,

$$D_{\mathrm{pod}} \;\geq\; C_f\, k_{\mathrm{pod}}\, \tfrac{1}{2}\rho V^2 S_{\mathrm{pod}} \tag{12}$$

$$C_f / m_{\mathrm{fac}} \;\geq\; \frac{0.455}{Re^{0.3}} \tag{13}$$

where $m_{\text{fac}} = 1.1$ is a margin factor to account for interference drag with the nearby wing, and where k_{pod} is the pressure-drag form factor approximated by[10]

$$k_{\text{pod}} \geq 1 + \frac{60}{(l_{\text{pod}}/2R_{\text{pod}})^3} + \frac{(l_{\text{pod}}/2R_{\text{pod}})}{400}. \tag{14}$$

For the zero-pod case (batteries placed inside the wing), the moment and bending calculations are implemented in the GP model exactly as described by Burton and Hoburg. If there are pods, the distributed shear load is offset by the pod weight at the location of the pod as shown in Figure 3. Specifically, at each spanwise location i which has a pod, the shear-load equation of the Burton and Hoburg model is modified here to

$$\mathcal{S}_{i+1} \geq \mathcal{S}_i + \frac{NW_{\text{cent}}/2}{S} \frac{c_{i+1} + c_i}{2} \Delta y - NW'_{\text{pod}} \tag{15}$$

where the new NW'_{pod} term is the concentrated total pod-weight (pod+battery) load. This produces the shear discontinuities shown in Figure 3.
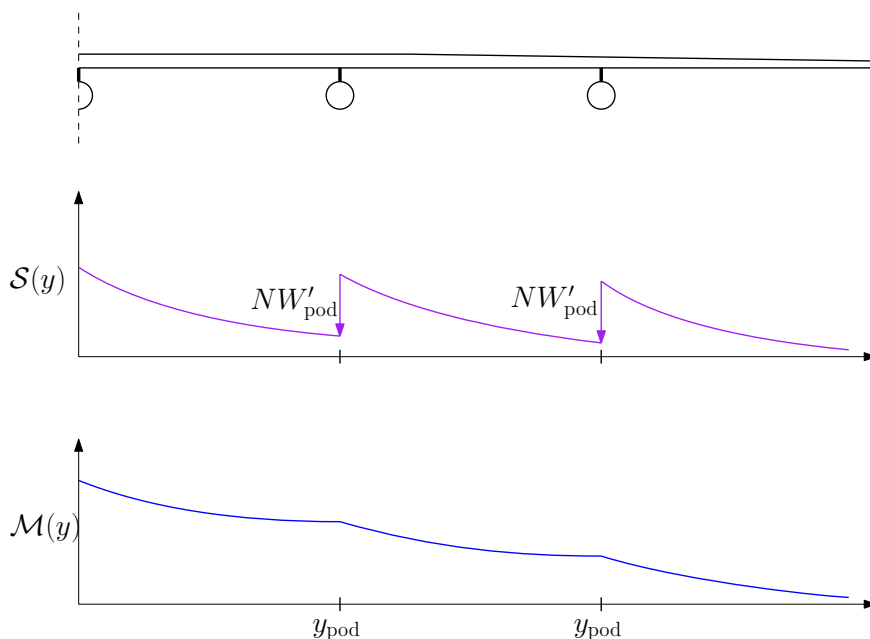
Figure 3: Shear and bending moment loads with outboard pods.

With these pod loads included in the wing beam model, the optimum solution captures the trade off between the bending relief from the pod weight loads and the added drag and weight of the pods. This analysis can also be used to quantify the benefit from having no pods vs one or more pods. Figure 4 shows the minimized takeoff weight for varying number of pods and with no pods. The overall aircraft weight is not very sensitive to the number of pods, so their use is attractive for the battery modularity and isolation they offer.

V. Resizing for Different Requirements

Because solar flux and wind speed vary with both season and latitude, it is not clear how aircraft size and weight would vary for different seasonal and latitude requirements. For the seasonal requirement, time is centered on the summer solstice such that 6-month availability corresponds to availability between March 21st and September 21st. Again using the solar GP model described by Burton and Hoburg, the model was solved 13 times for different requirements in a total of 2.67 seconds. Figure 5 shows the results of this study. Returned solutions for 10 and 12 month availability at 28° latitude were infeasible and therefore not shown.

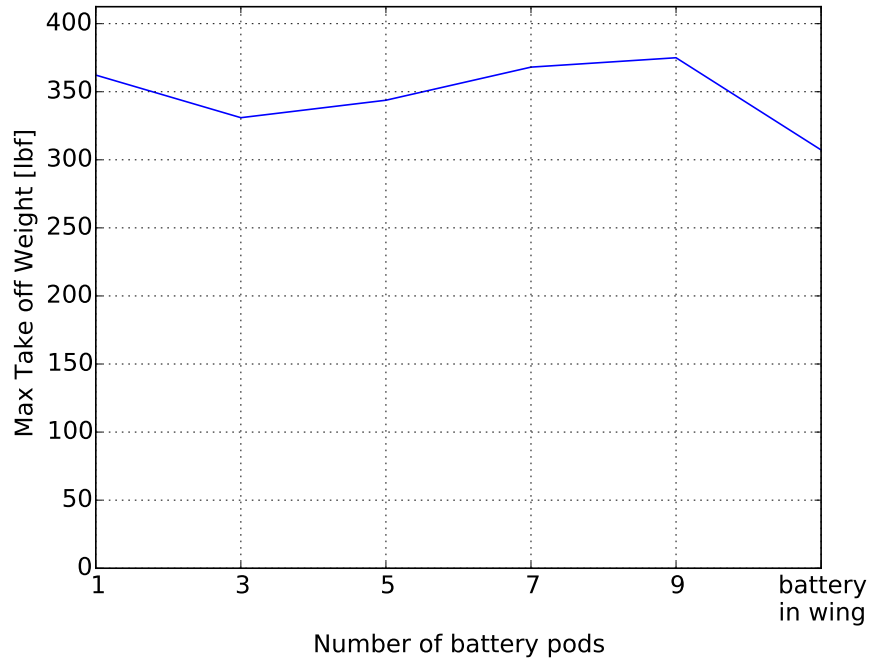American Institute of Aeronautics and Astronautics Paper 2018-XXXX

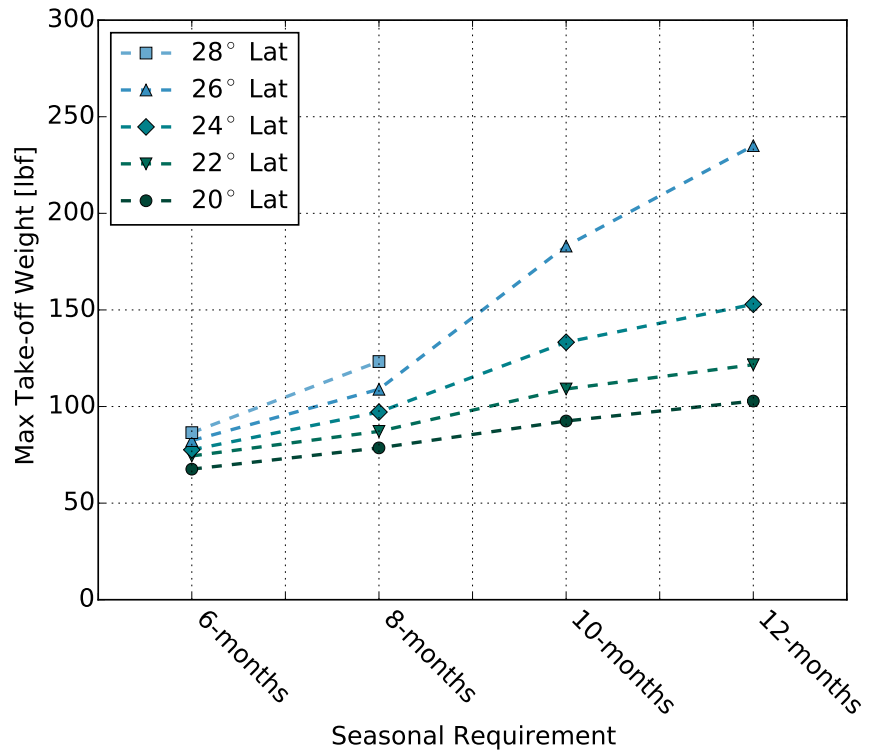**Figure 4: Maximum take off weight vs number of pods along the span.**

Figure 5: Resizing study for various latitude and seasonal requirements.

This trade study shows that different latitude and seasonal requirements can have drastic effects on aircraft size. Using these results as a baseline, a family of solar aircraft of various sizes and capabilities could

American Institute of Aeronautics and Astronautics Paper 2018-XXXX

be estimated to fulfill operational requirements.

VI. Tailboom Flexibility

Burton and Hoburg size the horizontal tail based on a specified tail volume coefficient [5]. However, for highly flexible aircraft, the horizontal tail effectiveness is decreased by the flexibility of the tailboom which must be countered by a greater horizontal tail area. The following model accounts for the tail effectiveness loss, and thus allows optimization of the tradeoff between the tailboom weight and the drag and weight of the horizontal tail.

A tube tailboom of diameter d has a total mass, root bending inertia, and bending stiffness distribution

$$m = \pi \rho_{\text{cfrp}} t_0 d l_{\text{h}} \left(1 - \tfrac{1}{2}k\right) \tag{16}$$

$$I_0 = \pi t_0 d^3/8 \tag{17}$$

$$EI(x) = EI_0 \left(1 - kx/l_{\text{h}}\right) \tag{18}$$

where the index $k = 0$ corresponds to a uniform wall thickness and stiffness, and $k = 1$ corresponds to linear dropoffs to zero. Intermediate k values correspond to partial linear dropoffs. When the tailboom is loaded at the endpoint $x = l_{\text{h}}$ by the horizontal tail lift L_{h}, the end deflection angle θ_{h} at the tail then follows from standard beam analysis.

$$\theta_{\text{h}} = \frac{L_{\text{h}} l_{\text{h}}^2}{EI_0} \frac{1+k}{2} = \frac{q S_{\text{h}} l_{\text{h}}^2}{EI_0} \frac{1+k}{2} C_{L_{\text{h}}} \tag{19}$$

The aircraft's overall pitching moment and corresponding coefficient, about the center of gravity, are

$$M_{cg} = M_{\text{w}} + (x_{cg} - x_{ac})L_{\text{w}} - l_{\text{h}} L_{\text{h}} \tag{20}$$

$$\frac{M_{cg}}{qSc} \equiv C_m = C_{m_{\text{w}}} + \frac{x_{cg} - x_{ac}}{c} C_{L_{\text{w}}} - V_{\text{h}} C_{L_{\text{h}}} \tag{21}$$

where we've assumed that the tailboom's effective root location is at the wing's aerodynamic center x_{ac}, and that the tail's pitching moment about its own aerodynamic center is negligible.

The moment and lift coefficients are approximated by

$$C_{m_{\text{w}}} = \text{constant} \tag{22}$$

$$C_L = C_{L_0} + m_{\text{w}} \alpha \tag{23}$$

$$C_{L_{\text{h}}} = C_{L_{\text{h}_0}} + m_{\text{h}} \left[\left(1 - \frac{d\epsilon}{d\alpha}\right)\alpha - \theta_{\text{h}}\right] \tag{24}$$

$$m_{\text{w}} = \frac{2\pi}{1 + 2/AR} \tag{25}$$

$$m_{\text{h}} = \frac{2\pi}{1 + 2/AR_{\text{h}}} \tag{26}$$

where in (24) both the wing downwash angle ϵ and the tailboom deflection angle θ_{h} both influence the tail lift. A bound-vortex representation for the high aspect ratio wing gives the following estimate for the wing downwash derivative.

$$\frac{d\epsilon}{d\alpha} = \frac{m_{\text{w}}}{4\pi} \frac{c}{l_{\text{h}}} \tag{27}$$

Combining equations (24) and (19) gives the direct relation between the tail lift coefficient and aircraft angle of attack,

$$C_{L_{\text{h}}} = \frac{m_{\text{h}}}{\mathcal{F}} \left(1 - \frac{d\epsilon}{d\alpha}\right)\alpha \tag{28}$$

$$\mathcal{F} = 1 + m_{\text{h}} \frac{q S_{\text{h}} l_{\text{h}}^2}{EI_0} \left(1 - \frac{k}{2}\right) \tag{29}$$

where $\mathcal{F}$ is a tailboom flexibility factor which decreases the tail's stabilizing power. The total pitching moment coefficient (21) and its derivative now become

$$
\begin{aligned}
C_m \;=\; C_{m_\mathrm{w}} \;&+\; \frac{x_{cg} - x_{ac}}{c}\left(C_{L_0} + m_\mathrm{w}\alpha\right) \\
&- \frac{V_\mathrm{h}}{\mathcal{F}} m_\mathrm{h}\left(1 - \frac{\mathrm{d}\epsilon}{\mathrm{d}\alpha}\right)\alpha
\end{aligned}
\tag{30}
$$

$$
\frac{\mathrm{d}C_m}{\mathrm{d}\alpha} \;=\; \frac{x_{cg} - x_{ac}}{c} m_\mathrm{w} \;-\; \frac{V_\mathrm{h}}{\mathcal{F}} m_\mathrm{h}\left(1 - \frac{\mathrm{d}\epsilon}{\mathrm{d}\alpha}\right).
\tag{31}
$$

Dividing this by $\mathrm{d}C_{L_\mathrm{w}}/\mathrm{d}\alpha = m_\mathrm{h}$ gives the static margin

$$
-\frac{\mathrm{d}C_m/\mathrm{d}\alpha}{\mathrm{d}C_{L_\mathrm{w}}/\mathrm{d}\alpha} \;=\; \mathrm{SM} \;=\; \frac{V_\mathrm{h}}{\mathcal{F}}\frac{m_\mathrm{h}}{m_\mathrm{w}}\left(1 - \frac{\mathrm{d}\epsilon}{\mathrm{d}\alpha}\right) \;-\; \frac{x_{cg} - x_{ac}}{c}.
\tag{32}
$$

The minimum required static margin is defined at the never-exceed dynamic pressure q_{NE} where the tailboom flexibility is most adverse, and when the c.g. is at its aft-most position.

$$
\mathrm{SM}_{\min} \;=\; \frac{V_\mathrm{h}}{\mathcal{F}_{NE}}\frac{m_\mathrm{h}}{m_\mathrm{w}}\left(1 - \frac{\mathrm{d}\epsilon}{\mathrm{d}\alpha}\right) \;-\; \frac{(x_{cg})_\mathrm{aft} - x_{ac}}{c}
\tag{33}
$$

Dividing equation (21) by C_{L_w} gives a requirement on the minimum (most negative) tail lift coefficient $(C_{L_\mathrm{h}})_{\min}$ required to achieve the pitch trim condition $C_m = 0$.

$$
0 \;=\; \frac{C_{m_\mathrm{w}}}{C_{L_\mathrm{w}}} \;+\; \frac{(x_{cg})_\mathrm{fwd} - x_{ac}}{c} \;-\; V_\mathrm{h}\frac{(C_{L_\mathrm{h}})_{\min}}{C_{L_\mathrm{w}}}
\tag{34}
$$

Adding (33) and (34) results in the horizontal tail sizing equation

$$
\mathrm{SM}_{\min} \;+\; \frac{\Delta x_{cg}}{c} \;-\; \frac{C_{m_\mathrm{w}}}{C_{L_{\max}}} \;\leq\; \frac{V_\mathrm{h}}{\mathcal{F}_{NE}}\frac{m_\mathrm{h}}{m_\mathrm{w}}\left(1 - \frac{\mathrm{d}\epsilon}{\mathrm{d}\alpha}\right) \;+\; V_\mathrm{h}\frac{-(C_{L_\mathrm{h}})_{\min}}{C_{L_{\max}}}.
\tag{35}
$$

where $\Delta x_{cg} = (x_{cg})_\mathrm{aft} - (x_{cg})_\mathrm{fwd}$ is the maximum allowable c.g. travel distance. This set of equations is GP compatible with the exception of Equations 25 and 35, which require signomial programming (SP) to solve. SP models solve a difference of convex programs as described by Boyd [6].

Table 4 shows relevant design variable values with and without the tailboom flexibility model. As expected, with the presence of tailboom flex the optimum (minimum weight) aircraft is heavier and has a larger horizontal tail surface area. The presence of tailboom flex also favors increasing the tailboom length, which is not obvious a priori.

Table 4: Effect of tail boom flexibility on design variables

Variable	Baseline Value	With Tail Flex
W_MTOW	436 lbf	418 lbf
V_h	0.45	0.132
l_h	25.4 ft	22.2 ft
S_h	23.3 ft^2	7.44 ft^2
W_h	2.38 lbf	0.737 lbf

VII.   Airfoil Thickness Trade Study

There is a trade off between structural efficiency and airfoil profile drag that is driven by the thickness of the airfoil. Increased thickness improves the y moment of inertia of the wing spar which improves wing stiffness and bending. However, increased thickness generally means higher profile drag. To capture this tradeoff in the GP model, a family of airfoils is evaluated for different Reynolds numbers and angles of attack
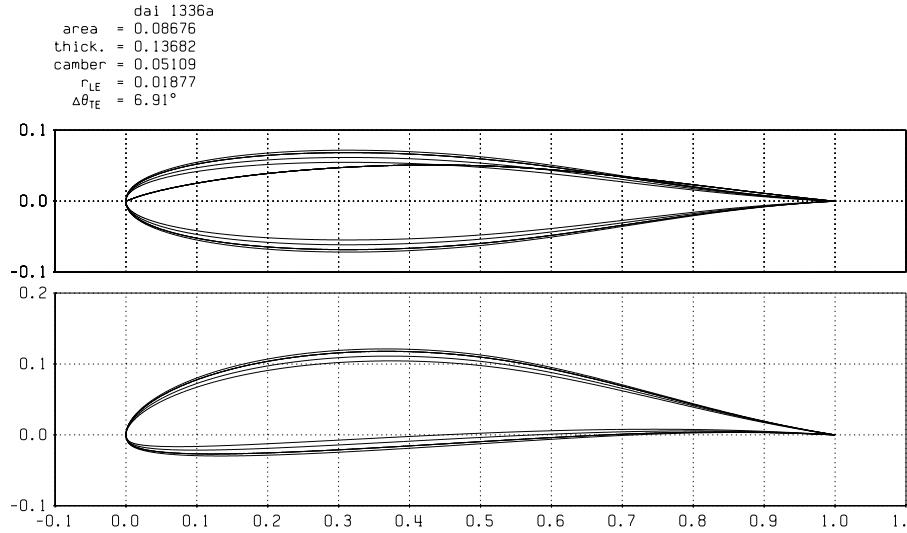
Figure 6: Airfoil family used to calculate fitted GP profile-drag function

in XFOIL. This data is fit to a posynomial function and incorporated into the GP model. The family of airfoils that is considered is scaled from the DAI1336 airfoil used for the Daedalus human-powered aircraft, and is shown in Figure 6.

The fitted function is outputs a profile drag coefficient as a function of thickness to chord ratio, Reynolds number, and lift coefficient

$$c_{d_p} \geq f(\tau, C_L, Re) \tag{36}$$

When incorporated into the overall model, each input is optimized for best performance. A portion of this fitted function is shown in Figure 7

As a practical matter the maximum thickness of the airfoil is constrained to be no greater than 0.144 to prevent poor stall characteristics at higher thicknesses. The maximum allowable thickness is an input parameter to the model and is varied to capture the sensitivity to that parameter. The resulting plot of maximum allowable thickness to aircraft weight is shown in Figure 8

VIII.   Propeller/Motor Sizing

A major tradeoff in a Solar HALE aircraft is the tradeoff between propeller efficiency, which favors a large prop diameter and low RPM, and motor weight which favors a small prop diameter and high RPM. Traditionally this tradeoff is performed by designing a sequence of prop/motor combinations for a specified thrust and varying propeller diameter, and then estimating the aircraft performance resulting from the efficiency and system weight of each combination. A considerable difficulty here is that each prop/motor combination will result in a different aircraft after re-optimization, so that the specified thrust is not completely known a priori. Here we will show that such design coupling between the prop, the motor, and the rest of the aircraft can be captured in a GP model, so that the entire system can be optimized simultaneously.

A.   Blade-Element Theory

The present formulation is that of QPROP [11], which is primarily the blade-element/vortex model of Betz [12] and Glauert [13], with a few modifications to improve accuracy at high disk loadings. The main development here is the re-casting of the QPROP model into a GP-compatible form.
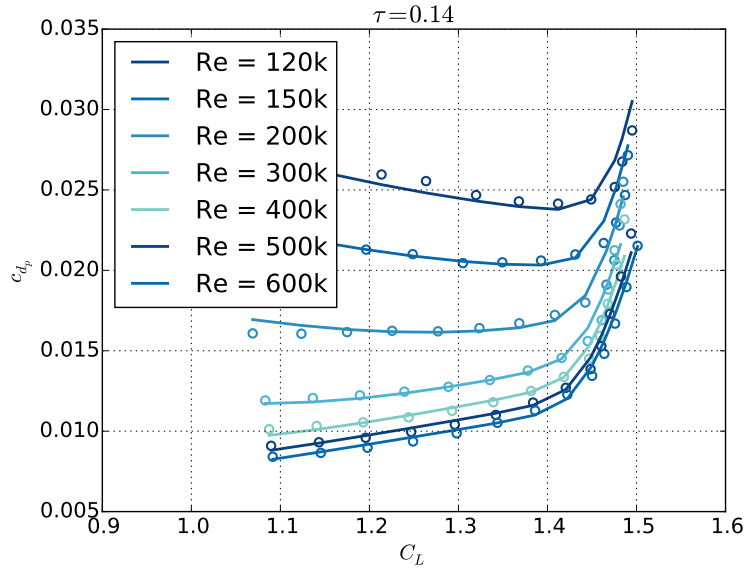
American Institute of Aeronautics and Astronautics Paper 2018-XXXX

Figure 7: Fitted GP equation to profile drag coefficient as a function of lift coefficient, Reynolds number, and thickness
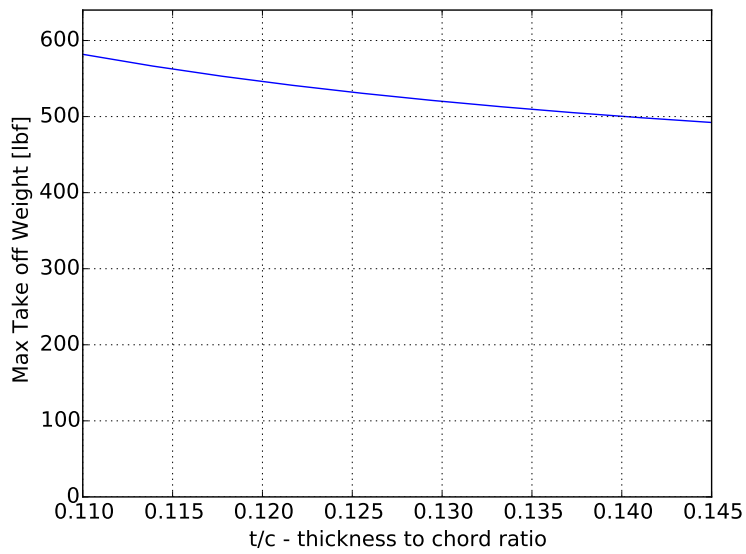

Figure 8: Maximum allowable thickness vs aircraft weight

Figure 9 shows the velocity triangle at some blade radius r. The total blade-relative speed W is formed from the total axial and tangential components W_a and W_t.

$$W_a \ \geq \ V \ + \ v_a \tag{37}$$

$$\Omega r \ \geq \ W_t + v_t \tag{38}$$

$$W \ = \ \sqrt{W_t^2 + W_a^2} \tag{39}$$

The total relative velocity W is constrained to be an equality in the solar aircraft model. This requires the use of the signomial programming extension of geometric programming, which is discussed in more detail in

American Institute of Aeronautics and Astronautics Paper 2018-XXXX
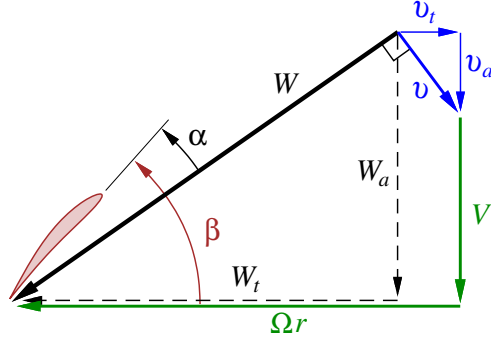
Figure 9: Velocities relative to propeller blade section at radial location r

[14]. The perturbation velocities v_a and v_t at the blade are associated with the propeller's trailing vorticity. The tangential component is related to the blade circulation at that radius by

$$v_t = \frac{B\Gamma}{4\pi r} \frac{1}{\bar{F}} \tag{40}$$

where $\bar{F}$ is a modified Prandtl tip correction factor which differs from the standard factor only over the inner radii.

$$\bar{F} = \frac{2}{\pi} \arccos(e^{-f}) \sqrt{1 + (4\lambda_w R/\pi B r)^2} \tag{41}$$

$$1 \geq \frac{2\lambda_w}{B} f + \frac{r}{R} \tag{42}$$

This formulation for $\bar{F}$ also requires signomial programming. A necessary modification here is the replacement of the $\arccos(e^{-f})$ term in (41) with the GP-compatible approximation

$$\arccos(e^{-f}) \approx 1.25\, f^{0.4587} \tag{43}$$

The accuracy of this approximation is discussed in Appendix A. The axial perturbation velocity is obtained from the other velocities by the assumption that it is orthogonal to the total velocity W.

$$v_a = v_t \frac{W_t}{W_a} \tag{44}$$

The kinematic relations above incorporate the local wake advance ratio defined by

$$\lambda_w = \frac{r}{R} \frac{W_a}{W_t} \tag{45}$$

which differs from the standard advance ratio $\lambda \equiv V/\Omega R$ by the inclusion of the propeller's own perturbation velocities. This modification improves accuracy for high disk loadings, and in particular it makes the model consistent with actual disk theory in the limit of infinite blades and zero advance ratio, $B \to \infty$ and $\lambda \to 0$.

The model is closed with the local Kutta-Joukowsky lift/circulation relation,

$$\Gamma = \frac{1}{2} W c\, c_l \tag{46}$$

and the blade airfoil lift and profile drag characteristics.

$$c_l \leq \min\left(\, c_{l_\alpha}\alpha + c_{l_0}\,,\ c_{l,max}\,\right) \tag{47}$$

$$c_d = c_d(c_l, Re) \tag{48}$$

$$Re = \frac{\rho\, W c}{\mu} \tag{49}$$

The $c_d(c_l, Re)$ function here is a posynomial fit to data generated by XFOIL. The accuracy of this fit is also discussed in Appendix A. The local angle of attack is obtained from the local velocity triangle,

$$\alpha = \beta - \arctan(W_a/W_t) \tag{50}$$

where β is the local blade angle.

The incremental thrust and torque of a radial blade interval Δr are given by

$$\Delta T \leq \rho B \Gamma (W_t - \epsilon W_a) \, \Delta r \tag{51}$$

$$\Delta Q \geq \rho B \Gamma (W_a + \epsilon W_t) \, r \, \Delta r \tag{52}$$

$$\epsilon = \frac{c_d}{c_l} \tag{53}$$

and the total thrust and torque defining constraints are obtained by summing over all the radial intervals.

$$T \leq \sum_{i=1}^{N} \Delta T_i \quad , \quad Q \geq \sum_{i=1}^{N} \Delta Q_i \tag{54}$$

The overall propeller efficiency is then

$$\bar{\eta} = \frac{V\,T}{\Omega\,Q} = \frac{V\,T}{P} \tag{55}$$

where $P = \Omega Q$ is the shaft power. We also define the local total efficiency

$$\eta = \frac{V\,\Delta T}{\Omega\,\Delta Q} = \frac{V}{\Omega r}\frac{W_t - \epsilon W_a}{W_a + \epsilon W_t} \tag{56}$$

which can be decomposed into induced and viscous (profile) efficiencies,

$$\eta = \eta_{\mathrm{i}}\,\eta_{\mathrm{v}} \tag{57}$$

$$\eta_{\mathrm{i}} = \frac{1 - v_t/\Omega r}{1 + v_a/V} \tag{58}$$

$$\eta_{\mathrm{v}} = \frac{1 - \epsilon\,W_a/W_t}{1 + \epsilon\,W_t/W_a} \tag{59}$$

which are used for optimum design, and are also useful for performance diagnosis.

B. Propeller analysis problem

As written, the relations above are suitable for the analysis problem where the blade geometry $c(r), \beta(r)$, typically defined at n discrete locations r_i, is specified. In addition specifying the flight speed V, and also one of Ω, T, or P, allows the blade circulations Γ_i to be computed and all other aerodynamic quantities then follow.

C. Propeller design problem

The design problem is also defined entirely by the above relations, but the inputs and outputs differ slightly. Specifically, in the design problem we determine the radial circulations Γ_i implicitly from the Minimum Induced Loss (MIL) condition,

$$1 - v_{t_i}/\Omega r_i = \bar{\eta}\,(1 + v_{a_i}/V) \quad ; \quad i = 1 \ldots n \tag{60}$$

$$T = T_{\mathrm{spec}} \tag{61}$$

where (60) requires that the local induced efficiency is constant everywhere and equal to one radially-constant value $\bar{\eta}$. This is analogous to specifying an elliptic loading shape on a wing. Setting ϵ to zero in (56) gives a GP-compatible expression for induced efficiency.

$$\bar{\eta} = \frac{V}{\Omega r}\frac{W_t}{W_a} \tag{62}$$

The MIL condition can then be met by adding the constraint

$$\bar{\eta}_i = \bar{\eta}_{i-1} \quad ; \quad i = 2 \ldots n \tag{63}$$

which will give the correct $c_l(r)$, $c(r)$, and $\beta(r)$ distributions.

D.   Propeller weight model

The propeller weight is assumed to scale linearly with thrust and area.

$$W_{\text{prop}} = T_{\text{max}}(R/R_W)^2 \tag{64}$$

The weight-reference radius $R_W = 50\,\text{ft}$ is calibrated based on the 11 ft diameter Daedalus human-powered aircraft propeller, which weighed 2 lbm and was stressed for 40 lbf of maximum static thrust. Any other posynomial weight model could be used here.

E.   Motor performance model

The motor performance model is also based on the QPROP formulation [15], with its equivalent circuit is shown in Figure 10. It assumes a constant motor resistance R_{motor}, a zero-load current i_0, and a motor speed constant K_V which is also used as the torque constant. The motor torque is assumed to be a function
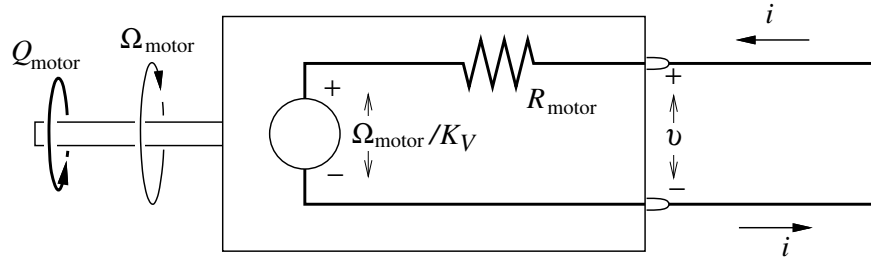
Figure 10: DC motor equivalent circuit

of the the current and speed constant, with some losses for motor friction.

$$Q_{\text{motor}} \geq (i - i_0)/K_V \tag{65}$$

The equivalent circuit gives the defining constraint for the motor terminal voltage v, in terms of the rotation rate Ω_{motor} and internal resistive voltage drop,

$$v \geq \frac{\Omega_{\text{motor}}}{K_V} + iR_{\text{motor}} \tag{66}$$

which then gives the motor electrical and shaft powers, and the corresponding efficiency.

$$P_{\text{elec}} = vi \tag{67}$$

$$P_{\text{motor}} = \Omega_{\text{motor}}Q_{\text{motor}} \tag{68}$$

$$\eta_{\text{motor}} = \frac{P_{\text{motor}}}{P_{\text{elec}}} \tag{69}$$

F.   Motor weight and parameter models

The design variables chosen to parameterize the motor are the motor weight W_{motor}, and the speed constant K_V. The motor parameters are W_1, which is a measure of motor power/weight technology, and i_{0_1}, which is a measure of motor windage and bearing losses. The motor parameters are then obtained by the relations

$$R_{\text{motor}} = \frac{W_1}{W_{\text{motor}}K_V^2} \tag{70}$$

$$i_0 = i_{0_1}K_V \tag{71}$$

which closely capture the characteristics across families of similar motors. The parameter values assumed here are $W_1 = 312\,\text{kg W/rpm}^2$, and $i_{0_1} = 0.01\,\text{W/rpm}$, obtained from the best-available large RC model motors. As for the prop weight model, any other posynomial models (with more parameters) could be used in lieu of the simple definitions above.

G. Motor-Propeller Integration

Without a gearbox the propeller and motor torque and speed are equal,

$$Q = Q_{\mathrm{motor}} \quad , \quad \Omega = \Omega_{\mathrm{motor}} \tag{72}$$

which strongly links the propeller and motor performance models. This allows the simultaneous design of a propeller and motor to meet some thrust requirement T_{spec} with no intermediate assumptions on available torque, rotation rate, and propeller geometry. The optimal balance between efficiency and weight is thus determined in the context of the entire aircraft system. This addresses the shortcoming in current propeller design methods discussed at the beginning of this section. Only a small number of fixed parameters are required; those related to motor internal losses, the blade airfoil sections, and number of propeller blades used.

IX. Vehicle Requirements Analysis

By incorporating the higher fidelity models described herein, the GP model can used to better estimate vehicle weight for different requirements for given technology assumptions. Figure 11 shows how vehicle weight trades off for different latitude requirements. Figure 12 shows contours of latitude for different
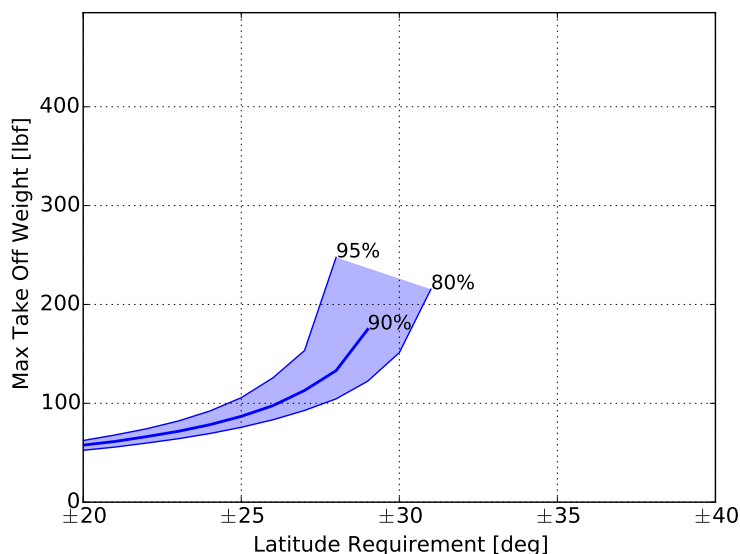

Figure 11: Vehicle weight vs latitude requirement

battery and solar technology assumptions. Figure 13 shows vehicle weight as a function of the number of propulsors and motor-weight technology parameter W_1. This shows it is most efficient to have a small number of larger propellers; the propeller efficiency decreases with propeller count. Finally, Figure 14 shows vehicle feasibility at different latitude for various payload requirements.

X. Conclusions

This paper described the use of GP to perform design parameter, configuration, and mission requirement trade studies for solar-electric powered aircraft. The inherent computational speed and robustness of existing GP solvers allows these trade studies to be performed very rapidly, which allows more extensive exploration of the design parameter space than would be possible with more conventional MDO methods. Furthermore, this paper demonstrates that models with higher fidelity than used in typical conceptual design procedures can be implemented with the GP framework, allowing development of relatively robust conceptual designs in a timely manner. The results are shown to capture important trends to guide conceptual and preliminary solar aircraft design. Specifically, it is observed that the box spars can significantly reduce aircraft weight. It is also shown through design sensitivities that improving battery technology will have a larger impact on
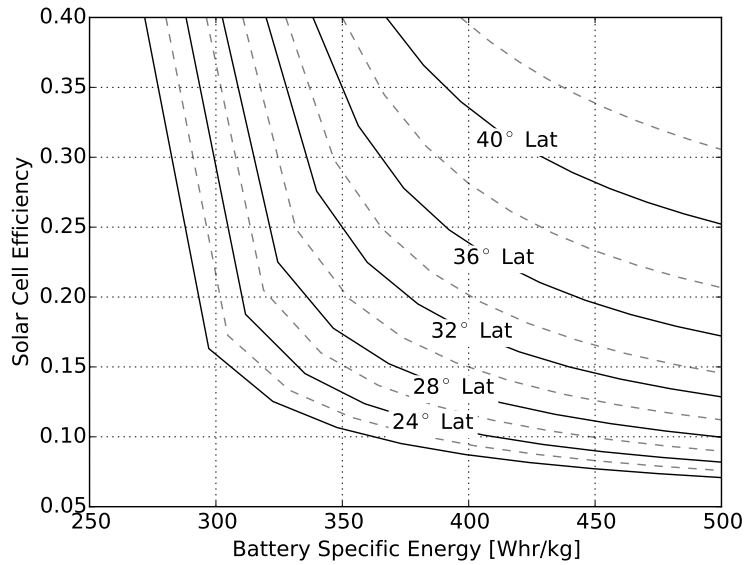
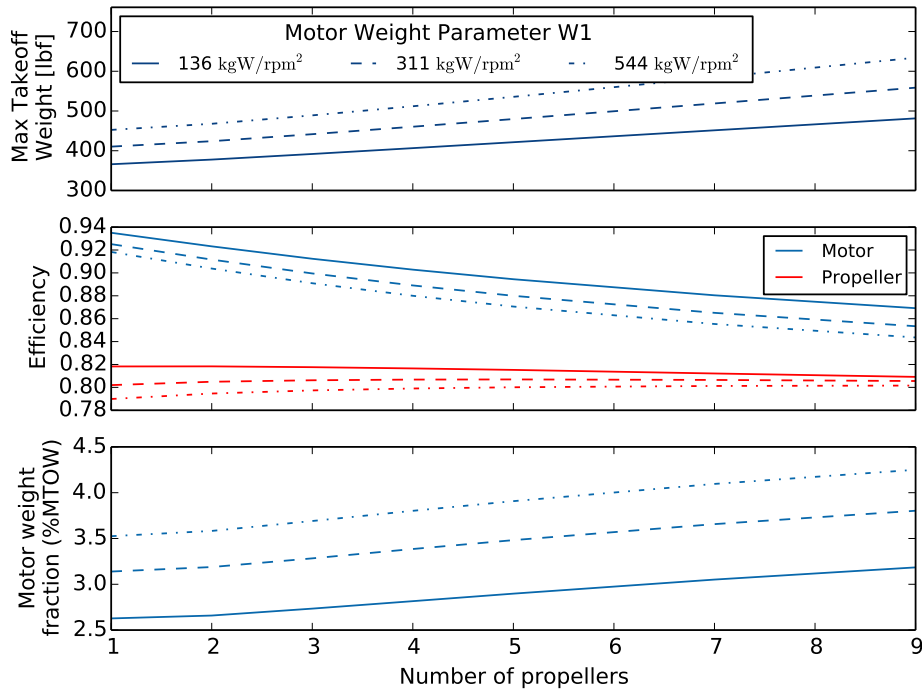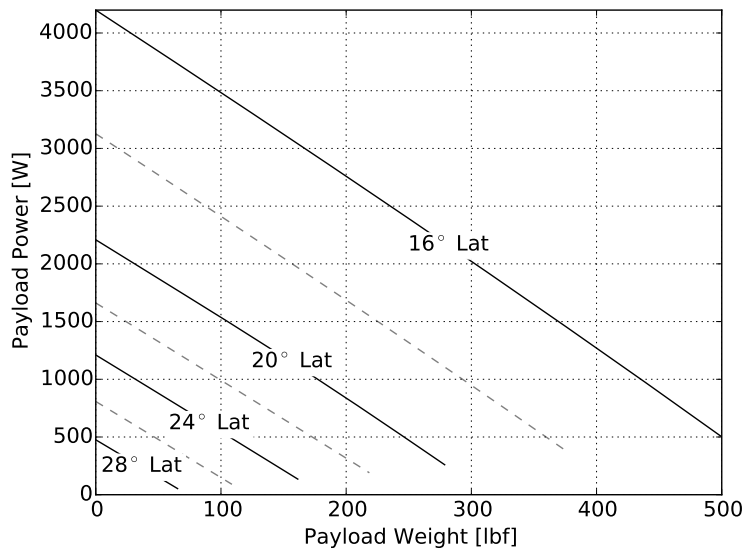**Figure 12: Vehicle weight vs latitude requirement**

Figure 13: Vehicle weight vs number of propulsors and motor-weight technology parameter

aircraft performance that improving solar cell efficiency. A resizing study shows that much smaller solar aircraft can be designed by relaxing latitude and seasonal requirements.

A. Geometric Programming Approximations

Periodic or non-convex functions can generally be fit with a suitable GP-compatible approximation over the relevant range of interest using the method outlined in [16]. In this paper two such approximations are used. The first is an approximation to the function $\arccos(e^{-x})$ over the range $0 < x \leq 3$, which is typical

Figure 14: Vehicle weight vs latitude requirement

for values in this model. The comparison of the fit with the exact values is shown in Figure 15. The RMS error for this fit is 0.067.
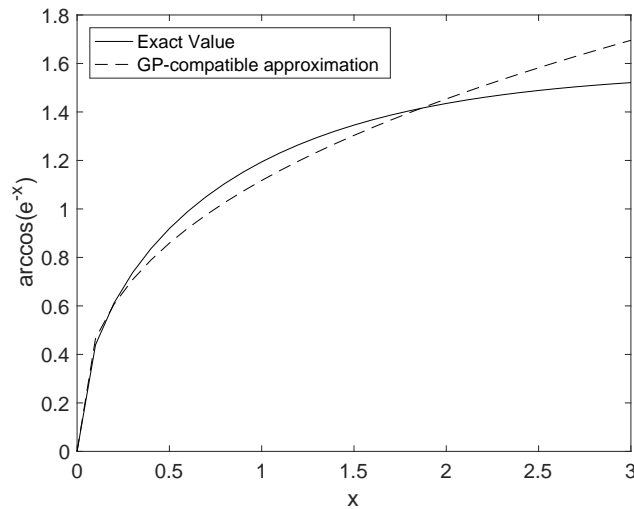

Figure 15: GP-compatible fit (dashed line) vs exact value (solid line) of $\arccos(e^{-x})$

The second is a fit of $c_d(c_l, Re)$ for the DAE51 propeller airfoil, used in the coupled propeller/motor model. Figure 16 shows the comparison of this fit (solid lines) with XFOIL results (open circles) across a relevant range of c_l and Re. This fit agrees reasonably well with the data, especially at lower c_l.

References

[1] Zuckerberg, M., "The technology behind Aquila," https://www.facebook.com/notes/mark-zuckerberg/the-technology-behind-aquila/10153916136506634/, jul 2016.

[2] G. Abbe, H. S., "Technological development trends in Solarpowered Aircraft Systems," *Renewable and Sustainable Energy Reviews*, Vol. 60, jul 2016, pp. 770–783.

[3] Martins, J. and Lambe, A., "Multidisciplinary Design Optimization: A Survey of Architectures," *AIAA Journal*, Vol. 51, No. 9, 2013, pp. 2049–2075.
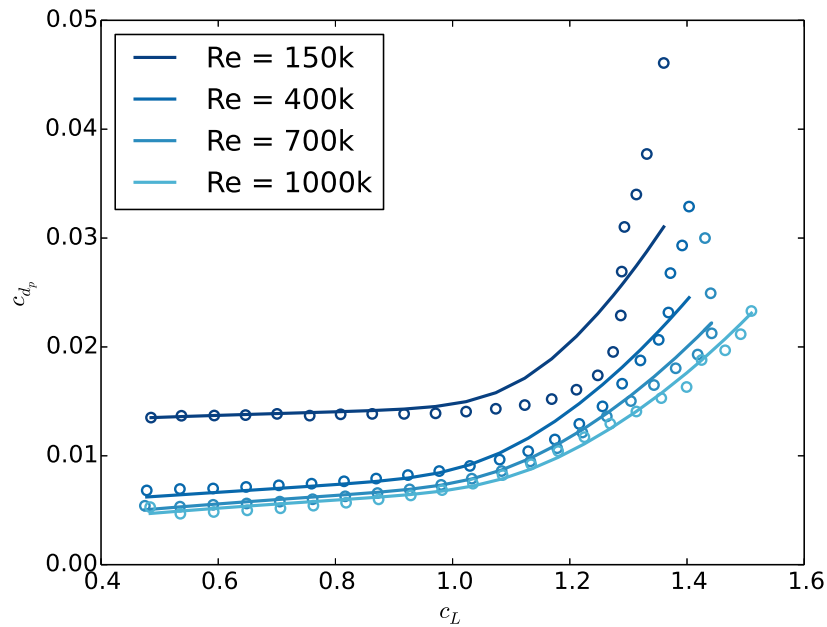
Figure 16: GP-compatible fit (solid lines) vs XFOIL simulation (open circles) of $c_d(c_l, Re)$ for the DAE51 propeller airfoil

^{4} Hoburg, W. and Abbeel, P., "Geometric Programming for Aircraft Design Optimization," *AIAA*, Vol. 52, No. 11, 2014, pp. 2414–2426.

^{5} Burton, M. and Hoburg, W., "Solar and Gas Powered Long-Endurance Unmanned Aircraft Sizing via Geometric Programming," *Journal of Aircraft*, Vol. 55, No. 1, 2018, pp. 212–225.

^{6} Boyd, S., S., K., L., V., and Hassibi, A., "A Tutorial on Geometric Programming," *Optimization and Engineering*, Vol. 8, No. 1, 2007, pp. 67–127.

^{7} Clearwater Composites, L., "Properties of Carbon Fiber," http://www.clearwatercomposites.com/resources/Properties-of-carbon-fiber, 2017.

^{8} Heckman, K., "Ellipsoid - Surface Area," https://www.vcalc.com/wiki/vCalc/Ellipsoid+-+Surface+Area, nov 2016.

^{9} Supply, F., "Carbon and Kevlar Fabrics," http://www.fiberglasssupply.com/Product_Catalog/Reinforcements/Carbon_and_Kevlar/carbon_and_kevlar.html, may 2016.

^{10} Raymer, D. P., *Aircraft Design: A Conceptual Approach*, American Institute of Aeronautics and Astronautics, Inc., 4th ed., 2006.

^{11} Drela, M., "QPROP Formulation," 2006.

^{12} Betz, A., "The Theory of the Screw Propeller," Technical Note 83, NACA, feb 1923.

^{13} Glauert, H., *Elements of Airfoil and Airscrew Theory*, Cambridge University Press, Cambridge, 1937.

^{14} Kirschen, P. G., Burnell, E. E., and Hoburg, W. W., "Signomial Programming Models for Aircraft Design," *AIAA SciTech*, 2016.

^{15} Drela, M., "First-Order DC Electric Motor Model," 2007.

^{16} Warren Hoburg, P. K., "Data fitting with geometric-programming-compatible softmax functions," *Optimization and Engineering*, 2016.